Applied Surface Science 640 (2023) 158088

Contents lists available at ScienceDirect

Applied Surface Science

journal homepage: www.elsevier.com/locate/apsusc

Full Length Article

Modulation the reaction paths of oxygen removal by electronic effects for $Fe_5C_2(100)$ surfaces

Huiyong Gong [a,b], Xiaoze Yuan [c], Ming Qing [b], Jinjia Liu [b], Xiao Han [a,b], Hong Wang [b,*], Xiao-Dong Wen [a,b,*], Yong Yang [a,b,*], Yongwang Li [a,b]

[a] State Key Laboratory of Coal Conversion, Institute of Coal Chemistry, Chinese Academy of Sciences, Taiyuan 030001, China
[b] National Energy Center for Coal to Liquids, Synfuels China Co., Ltd, Huairou District, Beijing 101400, China
[c] The State Key Laboratory of Nonlinear Mechanics, Institute of Mechanics, Chinese Academy of Sciences, Beijing 100190, China

ARTICLE INFO

Keywords:
Transition metals
Electronic effects
Oxygen removal
Electronegativity
Bonding analysis

ABSTRACT

This study employed spin-polarized density functional theory and investigated the removal of surface oxygen on $Fe_5C_2(100)$ surfaces substituted with first-row transition metals. It was observed that the substituted metals with lower electronegativity, such as Cr and Mn, could hinder the removal of surface oxygen. Conversely, substituted metals with higher electronegativity, such as Co, Ni, and Cu, facilitates the removal of surface oxygen. The results revealed a clear correlation between the energy barrier for oxygen removal and the electronegativity of substituted metals, which provides a straightforward and efficient approach to estimate the energy barrier for oxygen removal on iron carbide surfaces. Furthermore, the study demonstrated that the oxygen removal pathway is dependent on the electronegativity of substituted metals. For Cr and Mn substituted surfaces (low electronegativity), the oxygen removal via CO_2 pathway is preferable both in thermodynamics and kinetics, while for Cu substituted surfaces (high electronegativity), the hydrogenation of O to H_2O is more favorable. These findings reveal the significance of electronic promoters in catalyst design.

1. Introduction

In order to meet the growing demand for liquid fuels and comply with stringent environmental regulations, the selective conversion of syngas derived from carbonaceous resources (such as coal, natural gas, shale gas, or biomass feedstocks) into ultra-clean liquid fuels is considered as a viable alternative to address the growing energy and environment challenges [1–3]. The use of Fe-based catalysts has garnered significant attention from researchers worldwide due to their high efficiency, flexible process operation, and cost-effectiveness [4–6]. By adjusting the synthesis conditions, the precursor can be transformed into various iron carbides [7,8] which have been widely recognized as the active component among the different iron species [9,10]. Remarkably, Fe-based catalysts have demonstrated high conversion rates and excellent selectivity for heavy hydrocarbons, leading to their industrial implementation with a continuous production capacity of approximately 6.32 million tons in China [11–13]. However, their poor stability and rapid deactivation necessitate frequent replacement, resulting in a significant economic burden [6]. Therefore, understanding the deactivation mechanisms and developing high-tolerance catalyst designs are crucial.

Deactivation mechanisms reported for iron-based catalysts include poisoning [14,15], sintering [16], coking [17,18], and oxidation [15,19–21]. Among these, oxidation is considered a crucial deactivation mechanism [21,22]. One form of oxidation arises from the dissociation of carbon oxide, where dissociated chemisorbed oxygen strongly adsorbs onto specific sites, becoming difficult to remove. This results in the deactivation of surface sites and gradual oxidation of active species [23]. Another form of oxidation occurs through the re-adsorption of water molecules produced during the reaction. Under conditions of excess H_2O partial pressure and lower temperature, complete surface oxidation can occur, leading to irreversible oxidation [22,24]. H_2O vapor selectively adsorbs on active sites and releases oxygen atoms, a thermodynamically favorable reaction, causing the oxidation of iron carbides to Fe_3O_4 during the Fischer-Tropsch synthesis (FTS) process [25]. Consequently, enhancing the oxygen removal rate and improving the oxidation

* Corresponding authors at: State Key Laboratory of Coal Conversion, Institute of Coal Chemistry, Chinese Academy of Sciences, Taiyuan 030001, China (X.-D.W. and Y.Y.)
E-mail addresses: wanghong@synfuelschina.com.cn (H. Wang), wxd@sxicc.ac.cn (X.-D. Wen), yyong@sxicc.ac.cn (Y. Yang).

https://doi.org/10.1016/j.apsusc.2023.158088
Received 15 May 2023; Received in revised form 20 July 2023; Accepted 22 July 2023
Available online 22 July 2023
0169-4332/

resistance of iron carbides are crucial for achieving catalytic stability.

Promoters have the ability to combine with the active component, forming hybrid sites [26,27] or interface structure [28,29], thereby modulating the behavior of intermediate species and creating interfacial synergistic effects during oxygen removal. For instance, several studies have reported that Cu promoters can inhibit the oxidation of active sites by transferring H atoms to adjacent adsorbed oxygen species [30,31]. It has been demonstrated that Pt promoters can reduce the energy barrier for oxygen removal by adjusting the electron states of active sites [32]. Additionally, the addition of promoters can enhance the activity of the water–gas shift reaction, leading to the removal of H_2O molecules from the catalyst surfaces [33,34]. The adsorption energy and oxidation ability of H_2O molecules can be significantly weakened by pre-adsorbing carbon atoms or coating the catalyst with hydrophobic materials [24,35,36].

Despite the numerous strategies employed to enhance the removal of adsorbed oxygen and H_2O molecules, predicting the performance of oxygen removal based on electronic effects and experimentally modulating the reaction pathway remains challenging. Theoretical simulation offers a valuable approach to address this issue. In our previous study, we investigated the electronic effects of substituted sites on CO adsorption and activation [37]. In this paper, our objective is to gain insights into the electronic effects of substituted sites on oxygen removal and provide potential reaction pathways. To achieve this, we selected $Fe_5C_2(100)$ surfaces as the fundamental model, which represents one of the largest surfaces according to Wulff construction. Subsequently, we introduced substituted metals of first-row transition onto $Fe_5C_2(100)$ surfaces to simulate the electronic effects for oxygen removal, and different reaction paths were considered and compared. Finally, we analyzed the density of states (DOS) and crystal orbital Hamilton population (COHP) to elucidate the influence of electronic effects on oxygen removal.

2. Computation methods and models

2.1. Methods

All calculations were performed by using the plane-wave based density functional theory (DFT) method, coded in the Vienna Ab initio Simulation Package (VASP) [38,39]. The electron–ion interaction was described by the projector augmented wave (PAW) [40]. The spin-polarized generalized gradient approximation and Perdew-Burke-Ernzerhof function (GGA-PBE) were used to describe the electron exchange and correlation energy [41,42]. Spin-polarization was introduced for the magnetic properties of iron. The cut-off energy of plane wave basis was set to 400 eV. The atoms forces and electronic self-consistent interaction were set up to 0.03 eV/Å and 10^{-4} eV, respectively.

The adsorption energy (E_{ads}) of adsorbed species was calculated by the formulation defined as $E_{ads} = E_{X/slab} - E_{slab} - E_X$. Here, $E_{X/slab}$ is the total energy of the slab with the adsorbed species optimized to equilibrium state, E_{slab} is the total energy of the clean surface, and the E_X is the total energy of the free adsorbates in the gas phase. The energy barrier (E_a) was calculated by the formula of $E_a = E_{TS} - E_{IS}$ and the reaction energy (ΔE) was according to $\Delta E = E_{FS} - E_{IS}$, where E_{IS}, E_{TS}, and E_{FS} are the energy of adsorbed species consistent with the initial, transition and final states, respectively. The apparent energy barrier (E_{eff}) was the difference between the highest energy of reaction species and the energy of initial adsorption species on the potential energy surfaces. The transition states were located by the climbing image nudged band (CI-NEB) method, and the frequency analysis were executed to find the transition state exactly [43,44]. The zero-point energy (ZPE) correction were included in our reaction barriers and energies.

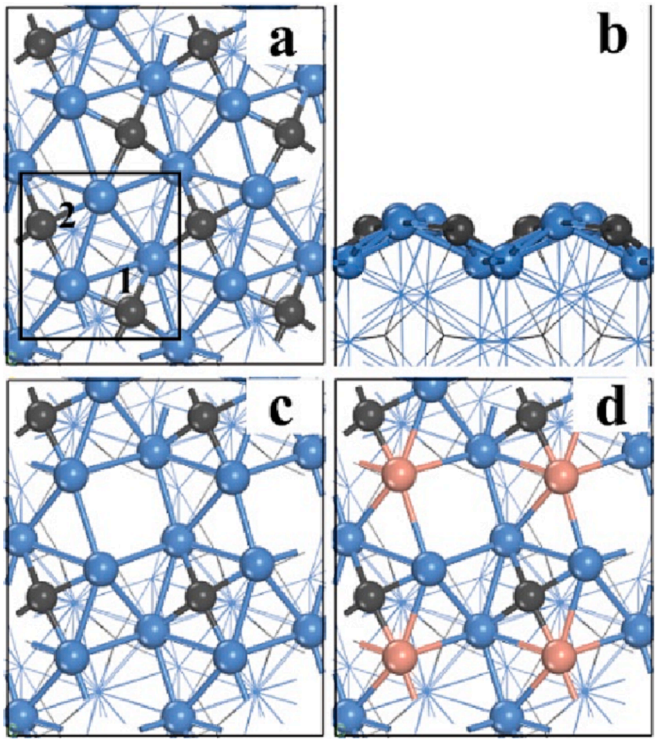

Fig. 1. Top (a) and side views (b) of perfect $Fe_5C_2(100)$ surface with 0.5 ML carbon coverage; top view of pure (c) and M substituted (d) $Fe_5C_2(100)$ surface with 0.25 ML carbon coverage. The blue spheres stand for Fe atoms, the black spheres for C atoms, orange sphere for M atoms. (For interpretation of the references to color in this figure legend, the reader is referred to the web version of this article.)

2.2. Models

According to the research of thermodynamic equilibrium for the Wulff construction, the surface of $Fe_5C_2(100)$ is one of the largest exposed surfaces under the FTS reaction conditions [45]. We chose p(2 × 2) slab model, which include 48 Fe atoms and 24 C atoms. For the perfect surface of $Fe_5C_2(100)$, there are 4 Fe and 2 C atoms in the unit cell and the coverage for C* is 0.5 ML, as displayed in Fig. 1a. Actually, the surface C* can be regarded as active atoms, which can participate in the elementary reaction and then give the vacant sites for next circulation. Based on that, the first C* were removed and the vacancy $Fe_5C_2(100)$ surfaces ($\theta_{C^*} = 0.25$ML) were constructed. One of the vacancy Fe atoms was substituted by other metal atom to study the electronic effects for oxygen removal, as shown in Fig. 1d. For the elementary reaction, the 20 top Fe atoms, 8 top C atoms and 4 top substituted atoms together with adsorbate were allowed to relax, while the other atoms were fixed. According to the lattice sizes, 2 × 2 × 1 k-point grid sampling within the Brillouin zones was set.

2.3. Bonding analysis and atomistic thermodynamics

The bonding interactions between adsorbate and adsorption sites were analyzed by density of state and the crystal orbital Hamilton population (COHP) [46–48].

The desorption reaction under a specific condition was studied by atomistic thermodynamics [49–51]. Here, we take CO_2 desorption on a $Fe_5C_2(100)$ surface, $CO_2/Fe_5C_2 \rightarrow Fe_5C_2 + CO_2$, as an example, and the change of Gibbs free energy (ΔG) can be described by equation (1).

$$\Delta G = G[Fe_5C_2(100)] + G_{gas}(CO_2) - G[(CO_2)/Fe_5C_2(100)] \quad (1)$$

For this equation, $G[Fe_5C_2(100)]$ is the Gibbs free energy of the clean

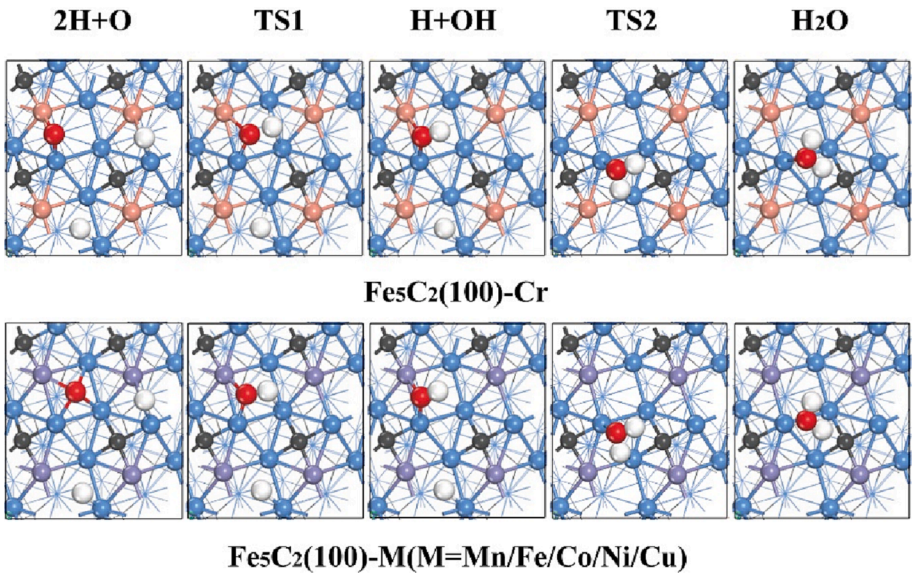

Fig. 2. Structure of consecutive hydrogenation process on the $Fe_5C_2(100)$−M (M = Cr/Mn/Fe/Co/Ni/Cu) surfaces. Black spheres for C, red spheres for O, white spheres for H, blue spheres for Fe, and other color spheres for the substitution M atoms. (For interpretation of the references to color in this figure legend, the reader is referred to the web version of this article.)

Table 1
Energetic data of oxygen removing via consecutive hydrogenation process for M modified $Fe_5C_2(100)$ surfaces.

surface	E_{ads}(IS)/ eV	$d_{(O-H)}$/Å	$d_{(HO-H)}$/Å	E_{a1}	E_{a2}	E_{eff}/ eV	ΔE/ eV
$Fe_5C_2(100)$−Cr	−2.15	1.359	1.409	0.84	2.13	2.62	2.20
$Fe_5C_2(100)$−Mn	−1.37	1.406	1.428	0.39	1.90	1.89	1.51
$Fe_5C_2(100)$−Fe	−1.28	1.443	1.447	0.46	1.79	1.74	1.32
$Fe_5C_2(100)$−Co	−1.15	1.459	1.471	0.51	1.62	1.57	1.19
$Fe_5C_2(100)$−Ni	−0.95	1.478	1.489	0.56	1.46	1.39	0.96
$Fe_5C_2(100)$−Cu	−0.52	1.515	1.466	0.50	1.30	1.04	0.51

$Fe_5C_2(100)$ surface, while $G[(CO_2)/Fe_5C_2(100)]$ is the Gibbs free energy of Fe_5C_2 surface with an adsorbed CO_2 molecule. Some approximations have been widely adopted by many researches for atomistic thermodynamics methods. The Gibbs free energy of the solid surfaces can be substituted by the energy calculated by DFT, owing to the negligible vibration contribution [52]. The $G_{gas}(CO_2)$ is equal to $\mu(CO_2)$. Thus, the chemical potential of CO_2 can be expressed as

$$\mu_{CO_2}(T, P) = E_{co_2}^{total} + \tilde{\mu}_{co_2}(T, P^0) + k_B T \ln(P_{CO_2}/P^0)$$

$E_{co_2}^{total}$ is the energy of isolated CO_2 gas-phase molecule, including the zero-point vibration. $\tilde{\mu}_{co_2}(T, P^0)$ is the chemical potential at different temperatures, and $k_B T \ln(P_{CO_2}/P^0)$ can be defined as the contribution of CO_2 partial pressure and temperature to the chemical potential. Thus, equation (1) can switch to

$$\Delta G = E[Fe_5C_2(100)] - E(CO_2)/Fe_5C_2(100)] + E_{co_2}^{total}$$

$$+ \tilde{\mu}_{co_2}(T, P^0) + k_B T \ln(P_{CO_2}/P^0)$$

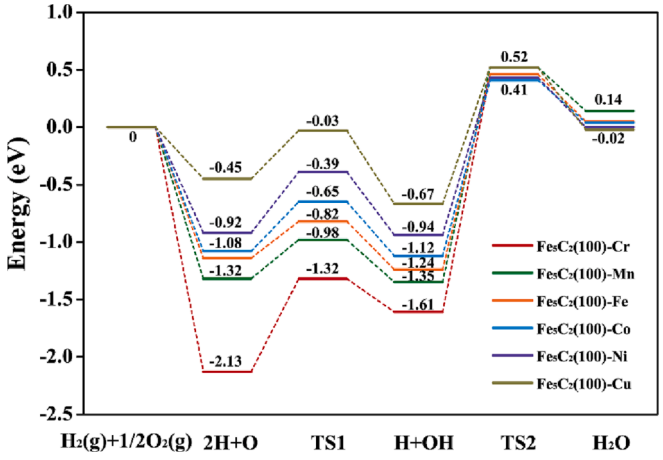

Fig. 3. Potential energy surfaces for oxygen removing via consecutive hydrogenation process on M modified $Fe_5C_2(100)$ surfaces.

3. Results and discussion

3.1. Oxygen removal by H_2O path

By conducting co-adsorption tests (Fig. S1, Supporting Information) of O and 2H, we identified the most stable adsorption configuration, which involves O atoms located on carbon vacancy sites and 2H atoms situated on adjacent carbon vacancy sites. Building upon this finding, we investigated the electronic effects of first-row transition metals on the successive hydrogenation-based removal of O.

Fig. 2 displays the geometries during the consecutive hydrogenation process for various transition metal substituted sites. There is a distinction in the initial state (IS) of the Cr substituted surface, where oxygen atoms are positioned on bridge sites, while for the other substituted surfaces, oxygen atoms adsorb on the substituted hollow sites. Across all surfaces, the OH species show a preference for adsorbing on the substituted bridge sites, while H_2O tends to adsorb on the top sites. Moreover, the geometries of the transition state (TS) are similar, owing to the comparable surface models and reaction pathway.

The co-adsorption energy of O and 2H is −1.28 eV for the pure

Table 2
Energetic data of oxygen removing via OH disproportionation for M modified $Fe_5C_2(100)$ surfaces, En is the Allen electronegativity of substituted atoms.

surface	E_{ads}(IS)/eV	E_{a1}	E_{a2}	E_{eff}/eV	ΔE/eV	En
$Fe_5C_2(100)$-Cr	−1.49	0.90	2.15	2.35	1.82	1.56
$Fe_5C_2(100)$-Mn	−1.38	0.51	1.92	1.82	1.65	1.60
$Fe_5C_2(100)$-Fe	−1.12	0.58	1.76	1.68	1.44	1.64
$Fe_5C_2(100)$-Co	−0.92	0.60	1.58	1.53	1.25	1.70
$Fe_5C_2(100)$-Ni	−0.73	0.65	1.42	1.38	1.01	1.75
$Fe_5C_2(100)$-Cu	−0.42	0.60	1.24	1.00	0.65	1.75

$Fe_5C_2(100)$, as displayed in Table 1. There is a slightly lower (0.09 eV) for Mn substituted surfaces, while it is sharply lowered by 0.78 eV for Cr substituted surfaces. However, contrary tendency is found for Co/Ni/Cu substituted surfaces. The co-adsorption energy increases by 0.13 eV for Co substituted surfaces and 0.33 eV for Ni substituted surfaces, respectively. On the Cu substituted surfaces, the co-adsorption energy dramatically increased to −0.52 eV.

As shown in Table 1, for all of the surfaces, the energy barrier (E_{a1}) is no more than 0.84 eV for the first step (O + H → OH) and they are slightly exothermic except for those substituted with Cr, which means that they are easy to form OH species. The transition state bond length of O–H ($d_{(O\text{-}H)}$) increased gradually from Cr to Cu substituted surfaces. In comparison with the first step, the second step (OH + H → H_2O) has higher energy barrier (E_{a2}) and are endothermic for all the surfaces (Fig. 3), forming the rate-limiting step of H_2O formation. It is also found that the transition state bond length of HO–H ($d_{(HO\text{-}H)}$) increased gradually from Cr to Ni substituted surfaces, which is corresponding to the change of energy barrier.

According to the co-adsorption of O + 2H, the apparent barrier (E_{eff}) and reaction energy (ΔE) were calculated, as displayed in Table 1. The apparent barrier and reaction energy of pure $Fe_5C_2(100)$ surfaces are 1.74 eV and 1.32 eV. By comparation, both the energy barrier and reaction energy increase by 0.88 eV for Cr substituted surfaces. The apparent barrier and reaction energy increase by 0.15 eV and 0.19 eV for Mn substituted surfaces, respectively. Those results indicate that H_2O formation are inhibited by Cr and Mn substituted surfaces. On the contrary, the energy barriers are lowered by 0.17 eV, 0.35 eV and 0.70

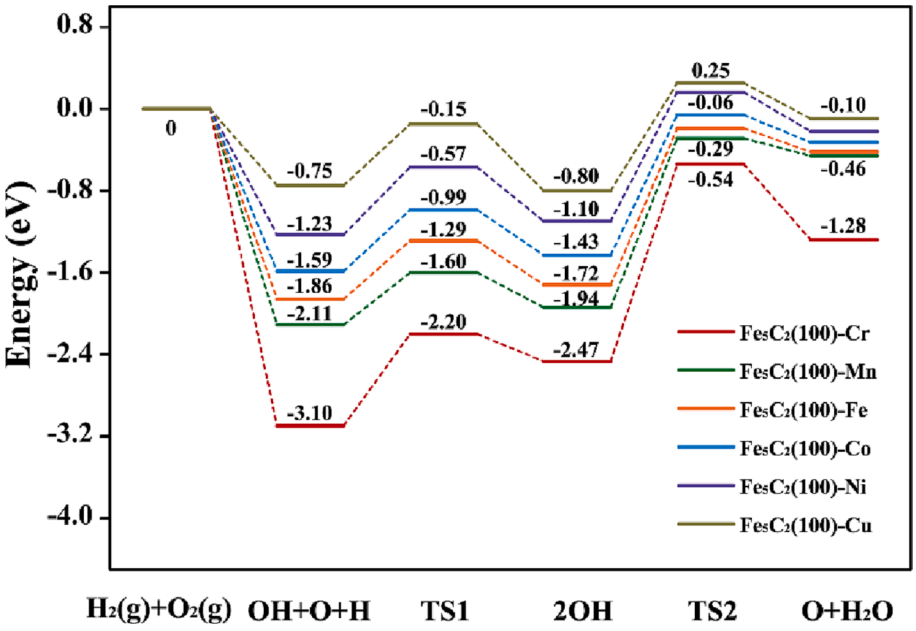

Fig. 4. Potential energy surfaces for oxygen removing via OH disproportionation on M modified $Fe_5C_2(100)$ surfaces.

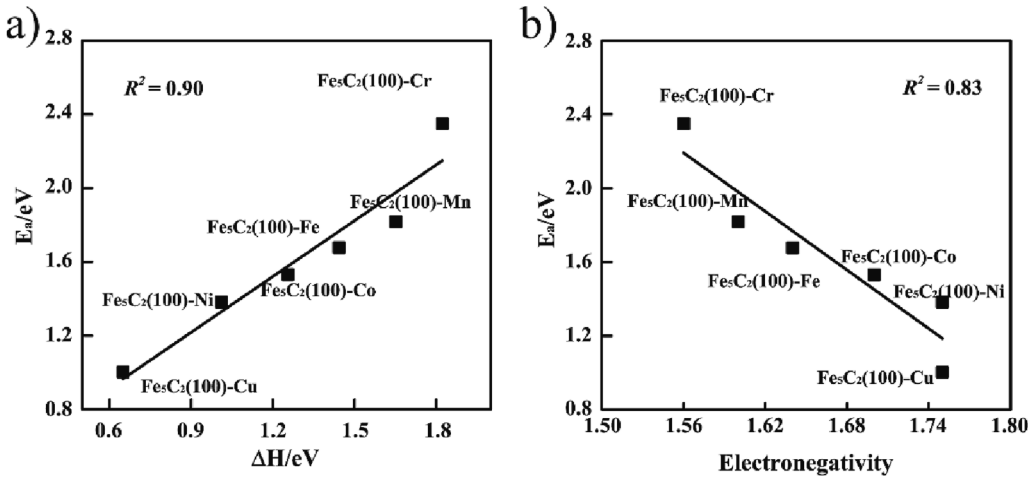

Fig. 5. The BEP relationship for oxygen removing via OH disproportionation (a), and the linear relation between oxygen removing barrier (E_{eff}) and the electronegativity of substituted atoms (b).

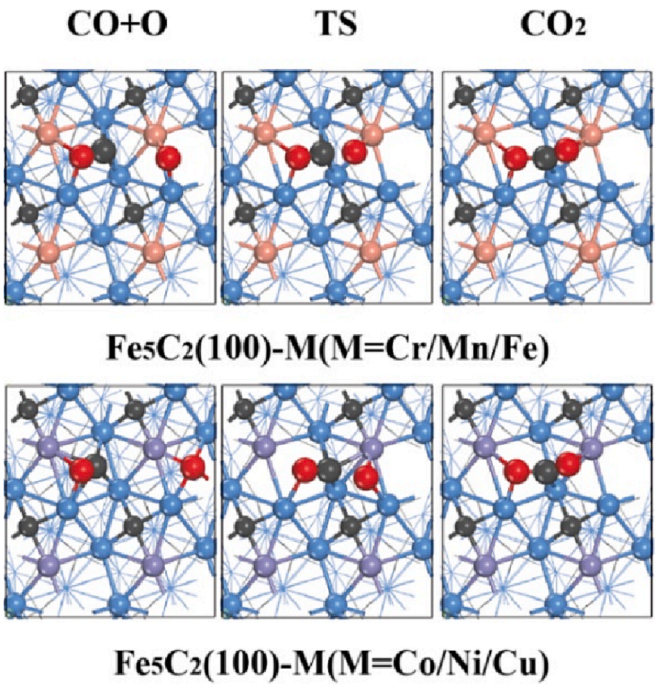

Fig. 6. Structure of oxygen removing via CO_2 path on M modified $Fe_5C_2(100)$ surfaces.

eV, and the reaction energy are lowered by 0.13 eV, 0.36 eV and 0.81 eV for Co, Ni, Cu substituted surfaces, respectively, which indicate that the formation of H_2O is thermodynamically favored. Therefore, the performance for oxygen removing follows the following trend: $Fe_5C_2(100)$−Cr < $Fe_5C_2(100)$−Mn < $Fe_5C_2(100)$− Fe < $Fe_5C_2(100)$−Co < $Fe_5C_2(100)$−Ni < $Fe_5C_2(100)$−Cu. Among all the modified surfaces, the Cu modified surface stands out with the optimal performance.

Alternatively, the OH disproportionation process was also considered for surface oxygen removal (OH + O + H → H_2O + O). The geometries of OH disproportionation process for different transition metal dopants are shown in Fig. S2 and the energetic data are displayed in Table 2. The energy barriers (E_{a1}) of the first step (OH + O + H → 2OH) fall into the range of 0.51−0.90 eV, with the highest energy barrier for Cr substituted surfaces, indicating OH species are easy to form. As the rate-limiting step of H_2O formation, the second step (2OH → H_2O + O) has higher energy barrier (E_{a2}) and are endothermic for all the surfaces (Fig. 4). The apparent barrier (E_{eff}) and reaction energy (ΔE) were also calculated, as showed in Table 2. Compared with the consecutive hydrogenation process, the energy barrier is lowered largely for Cr substituted surfaces (2.35 eV vs 2.62 eV), while the energy barrier is only slightly lowered for other substituted surfaces. Conversely, the reaction energy is improved to some extent for OH disproportionation process except Cr substituted surfaces. By comparing two reaction paths (Table S1), we can find that OH disproportionation process is kinetically favorable and consecutive hydrogenation process is thermodynamically advantageous. Therefore, Cr substituted surfaces are more likely to undergo the OH disproportionation pathway, while other substituted surfaces may undergo either a disproportionation reaction (2OH → H_2O + O) or consecutive hydrogenation (O + 2H → H_2O).

According to the computed energy data for all the modified surfaces, relationships between the energy barrier and the reaction energy or the energy barrier and metal electronegativity can be established and analyzed. The Brønsted–Evans–Polanyi (BEP) relationship was examined, as displayed in Fig. 5a. There is a good linear relationship between the energy barrier and the reaction energy (R^2 = 0.90), which may be attributed to the similar adsorption configuration and reaction path. Furthermore, the effect of metal electronegativity on the energy barrier

Table 3
Energetic data of oxygen removing via CO_2 path for M modified $Fe_5C_2(100)$ surfaces.

surface	E_{ads}(IS)/eV	$d_{(C\text{-}O)}$/Å	E_a/eV	ΔE/eV
$Fe_5C_2(100)$−Cr	−3.62	1.761	1.67	1.12
$Fe_5C_2(100)$−Mn	−2.95	1.810	1.52	0.84
$Fe_5C_2(100)$−Fe	−2.52	1.833	1.47	0.72
$Fe_5C_2(100)$−Co	−2.13	1.848	1.34	0.59
$Fe_5C_2(100)$−Ni	−1.88	1.881	1.34	0.62
$Fe_5C_2(100)$−Cu	−1.33	1.951	1.16	0.37

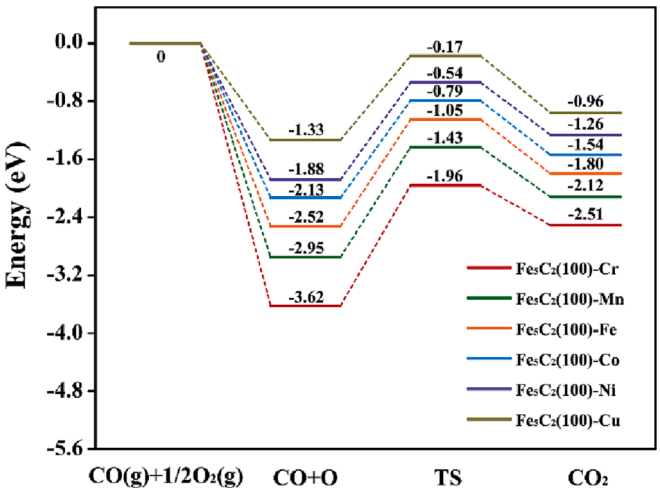

Fig. 7. Potential energy surfaces for oxygen removing via CO_2 path on M modified $Fe_5C_2(100)$ surfaces.

of H_2O formation was investigated (Table 2). The surfaces substituted by the lower electronegativity element of Cr and Mn show higher energy barrier, while the surfaces with higher electronegativity element of Co, Ni and Cu, exhibit lower energy barrier. The negative correlation was established between element electronegativity and apparent energy barrier, as displayed in Fig. 5b, suggesting that the energy barrier of H_2O formation decreases with the increase of substituted elements electronegativity.

3.2. Oxygen removal by CO_2 path

For the co-adsorption of CO and O, two adsorption configurations were examined. As shown in Fig. S3, one is that CO is adsorbed on the hollow sites and O atoms are located on the substituted bridge sites, the other is that CO is adsorbed on the hollow sites and O atoms are located on adjacent carbon vacancy with four coordination. The calculation results indicate that the bridge adsorption is dominant for Cr/Mn/Fe substituted surfaces, while the hollow adsorption is more stable for Co/Ni/Cu substituted surfaces (Table S2). The bridge adsorption configuration was considered as the initial configuration for Cr/Mn/Fe substituted surfaces, while the hollow adsorption configuration was adopted for Co/Ni/Cu substituted surfaces (Fig. 6).

As exhibited in Table 3, the co-adsorption energy (E_{ads}) of CO and O is −2.52 eV for the pure $Fe_5C_2(100)$. Compared with the pure $Fe_5C_2(100)$ surface, the co-adsorption energy for Cr and Mn substituted surfaces are decreased by 1.1 eV and 0.43 eV, respectively. On the contrary, the co-adsorption energy is increased by 0.39 eV and 0.64 eV for Co and Ni substituted surfaces, respectively. Much lower co-adsorption energy was obtained for the Cu substituted surfaces, which increase by 1.19 eV dramatically.

As for the activation energy (E_a) of oxygen removing by CO, it is 1.47 eV for the pure $Fe_5C_2(100)$ surface, which is in line with the reported results [53]. The similar case, like oxygen removal by H_2O path, was

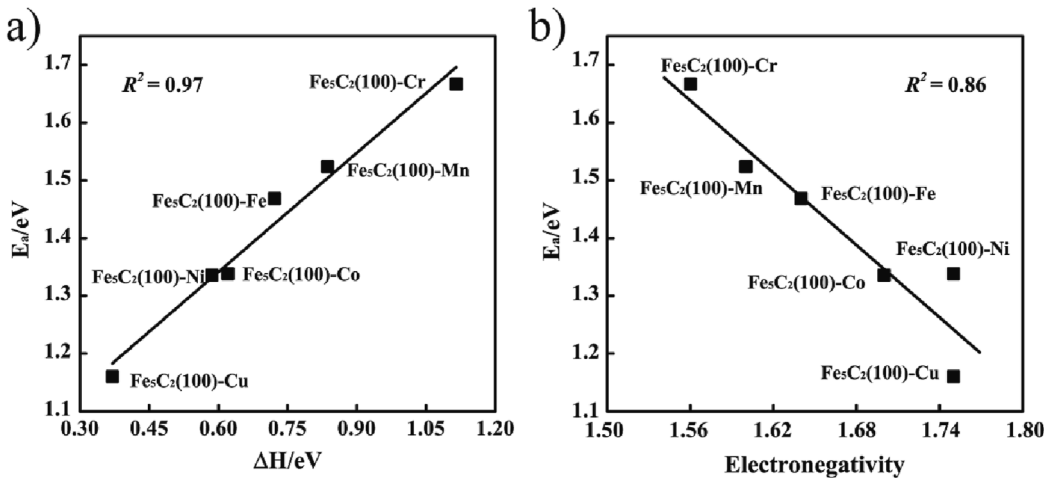

Fig. 8. The BEP relationship (a) for oxygen removal and the linear relation between oxygen removal barrier (E_a) and the electronegativity (b) of M atoms.

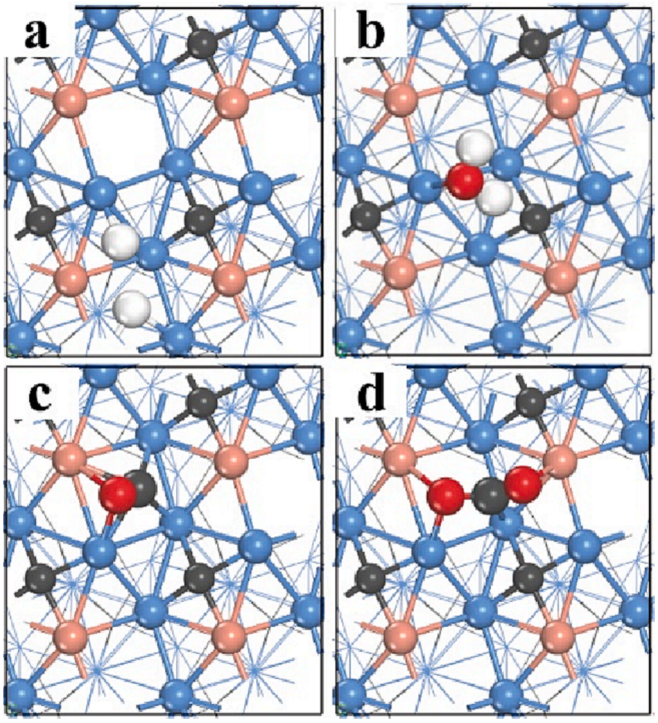

Fig. 9. Adsorption configuration for gas molecular: (a) H_2, (b) H_2O, (c) CO, (d) CO_2.

found that the surfaces substituted by Cr and Mn inhibit the removal of adsorbed oxygen by increasing the energy barrier of 0.2 eV and 0.05 eV, respectively (Table 3 and Fig. 7). The oxygen removal energy barrier is lowered by 0.13 eV equally for Co and Ni substituted surfaces and by 0.31 eV for Cu substituted surfaces, indicating that they promote the removal of adsorbed oxygen atoms. Meanwhile, the increase of C−O transition states bond length ($d_{(C\text{-}O)}$) from Cr to Cu substituted indicates that the bonding is enhanced progressively.

As displayed in Fig. 7, the reaction of oxygen removing via CO_2 path for all the substituted surfaces are endothermic. Relative to the pure Fe_5C_2(100) surface, the reaction energy (ΔE) is increased by 0.4 eV for Cr substituted surfaces and 0.12 eV for Mn substituted surfaces, respectively. This indicates that oxygen removal via CO_2 path is thermodynamically inhibited. Conversely, the reaction energy is lowered by 0.13 eV, 0.10 eV and 0.35 eV for Co, Ni, Cu substituted surfaces, respectively, promoting the removal of adsorbed oxygen thermodynamically.

Based on the relevant energy data for oxygen removing by CO_2 path, as showed in Fig. 8, there is also a good linear relationship between energy barrier and reaction energy, which conforms the BEP relationship with R^2 of 0.97. The relationship provides a way to evaluate the energy barrier quickly from data of IS and FS. In addition, the relationship between energy barrier and electronegativity was examined, which displays as negative correlation with R^2 of 0.86. This relationship provides the possibility to assess the energy barrier from the characteristic of substituted metal conveniently (see Fig. 8).

Subsequently, we compared the energy barrier and reaction energy of oxygen removal by CO_2 with H_2O. The CO_2 path is dominant both kinetically and thermodynamically for all the substituted surfaces except Cu substituted surfaces. For Cu substituted surfaces, the oxygen removal by H_2O is preferred kinetically, indicating that Cu could promote the reduce of Fe-based catalysts [31,54].

3.3. Desorption temperature

As shown in Fig. 9, CO is located on the hollow sites and H_2 dislocated adsorption on the adjacent vacancy, while CO_2 is located on the B5 sites and H_2O located on the top sites. According to the adsorption energy or energy barrier, the desorption temperature of CO, CO_2, H_2 and H_2O on the substituted surfaces at ultra-high vacuum (UHV) conditions were computed. Because it is easy to dissociation, the H_2 dissociation adsorption energy was used to calculate the desorption temperature. As shown in Table S3, the adsorption energy of H_2O is very low, so the desorption temperature dose not be controlled by the H_2O desorption. Instead, the desorption temperature of H_2O was computed by the rate-determining step barrier ($OH + H \rightarrow H_2O$) [35]. For CO_2 desorption, the adsorption energy is lower than the energy barrier of CO_2 formation, so the desorption temperature of CO_2 was also computed by the energy barrier ($O + CO \rightarrow CO_2$).

As shown in Fig. 10, the H_2 desorption temperature of 365 K is very close to the experiment of 315 K [35,55]. Comparatively, Cr/Mn substituted surfaces increase the dissociation adsorption energy and improve the desorption temperature. The desorption temperature was lowered by Cu substituted surfaces, which is attributed to the higher ability to activate H_2. The H_2O desorption temperature of 668 K is very close to the experiment of 623–800 K [56,57]. The desorption temperature increases for Cr/Mn substituted surfaces, while it is decreased by Co/Ni/Cu substituted surfaces. The formation of H_2O is endothermic and the energy barrier is higher than the adsorption energy of H_2, so the high temperature and high H_2 partial pressure are indispensable for the removal of the surface oxygen. The CO adsorption energy decreases

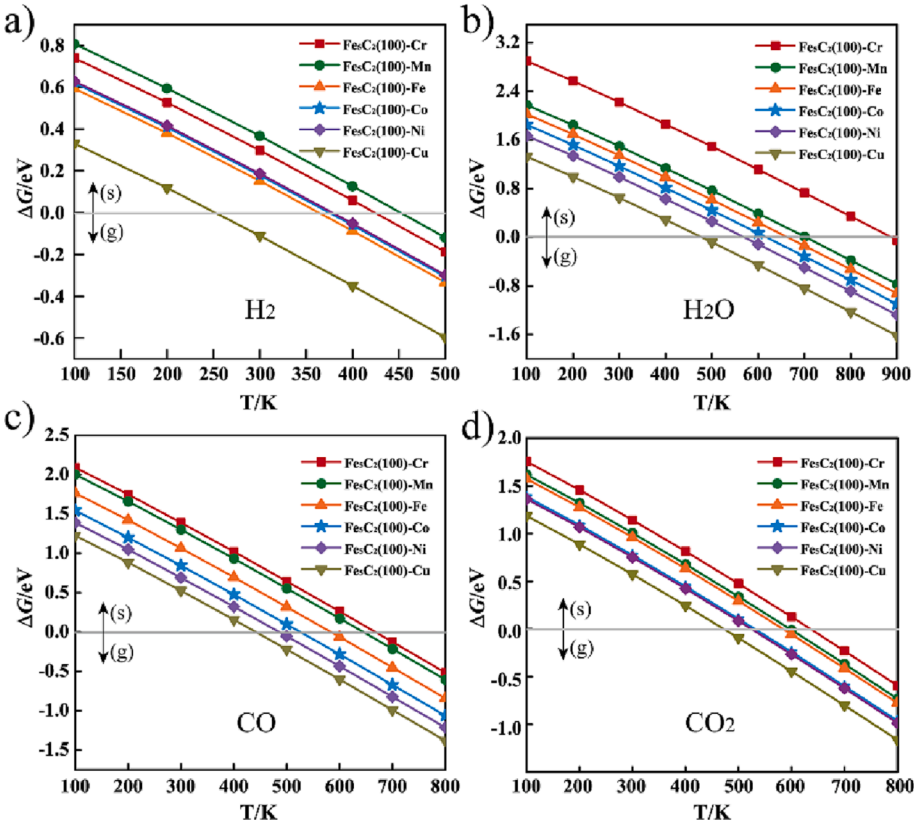

Fig. 10. Desorption temperature at 1 × 10^{-6} Pa on M modified Fe_5C_2(100) surfaces: (a) H_2, (b) H_2O, (c) CO, (d) CO_2.

progressively from Cr to Cu, and the desorption temperature falls in the range of 440−680 K. The CO_2 desorption temperature is much lower than the desorption temperature of H_2O for the Cr/Mn/Fe substituted surfaces, indicating that lower temperature was needed to remove the surface oxygen by CO_2 path.

3.4. Electronic effects analysis

The partial density of states (pDOS) and the crystal orbital Hamilton population (COHP) were performed to gain insight into the underlying mechanism of electronic effects modified by transition metals for oxygen removal. For convenience, the −(pCOHP) was used so that the positive values correspond to the bonding. As shown in Fig. 11, the band structures and bonding analysis of adsorption oxygen on substituted sites were carried out. Though they have the similar configuration and coordination environment, many differences from pDOS and pCOHP analysis can be found. The 3d orbitals of the substituted metals shift to the lower energy from Cr to Cu atoms, which is consistent with the law of d-band center theory. The interaction can be characterized by the overlap of state density between 2p orbitals of oxygen and 3d orbitals of substituted metals. Compared with Fe substituted surfaces, the larger overlap for Cr/Mn substituted surfaces indicates a strong interaction, while the smaller overlap for Cu substituted surfaces illustrates a weak interaction. Furthermore, the strength of interaction can also be testified by bonding analysis of COHP. The Cr/Mn substituted surfaces have higher Cr−O/Mn−O bonding intensity and wider bonding region. However, the bonding strength is weakened and bonding region is reduced for Co/Ni/Cu substituted surfaces. The analysis indicates that the interaction between the surfaces and adsorbed oxygen is enhanced by Cr and Mn substituted surfaces, which increases the adsorption energy and oxygen removal energy barrier. On the contrary, the interaction between surfaces and adsorbed oxygen is weaken by Co/Ni/Cu substituted, which decreases the adsorption energy and promotes the removal of adsorbed oxygen.

4. Conclusions

In summary, this study aimed to gain insight into the mechanism of surface oxygen removal and explore the electronic modulation by investigating the process of surface oxygen removal on Fe_5C_2(100) surfaces modified with different metals using spin polarized density functional theory.

Compared to the pure Fe_5C_2(100) surface, Cr/Mn substituted has been observed to enhance the adsorption of surface oxygen, while Co/Ni/Cu substituted weakens surface oxygen adsorption to varying degrees. In terms of the removal of oxygen from the surface, Cr/Mn substituted exhibits a negative effect on promoting oxygen removal, whereas Co, Ni, and Cu substituted decrease the energy barrier for oxygen removal. The relationship between the energy barrier and reaction energy follows the Brønsted–Evans–Polanyi principle, and a correlation has been established between the energy barrier for oxygen removal and the electronegativity of the substituted metal. These relationships offer a convenient means to estimate the energy barrier for oxygen removal.

A comparison of the results between the H_2O path and CO_2 path reveals that oxygen removal predominantly occurs via the CO_2 path on Cr/Mn substituted surfaces. For Fe/Co/Ni substituted surfaces, both paths are possible, although the system may shift towards the H_2O path on Cu substituted surfaces due to a lower energy barrier. The analysis of electronic effects suggests a stronger bonding interaction between the adsorbed oxygen and Cr/Mn substituted surfaces. However, the bonding strength considerably weakens on Cu substituted surfaces.

The findings of this study provide valuable insights into the electronic effects involved in surface oxygen removal. These insights can be highly instructive for catalyst design, as they enable the manipulation of oxygen removal pathways based on electronic effects. This knowledge can be leveraged to optimize catalyst performance and enhance catalytic

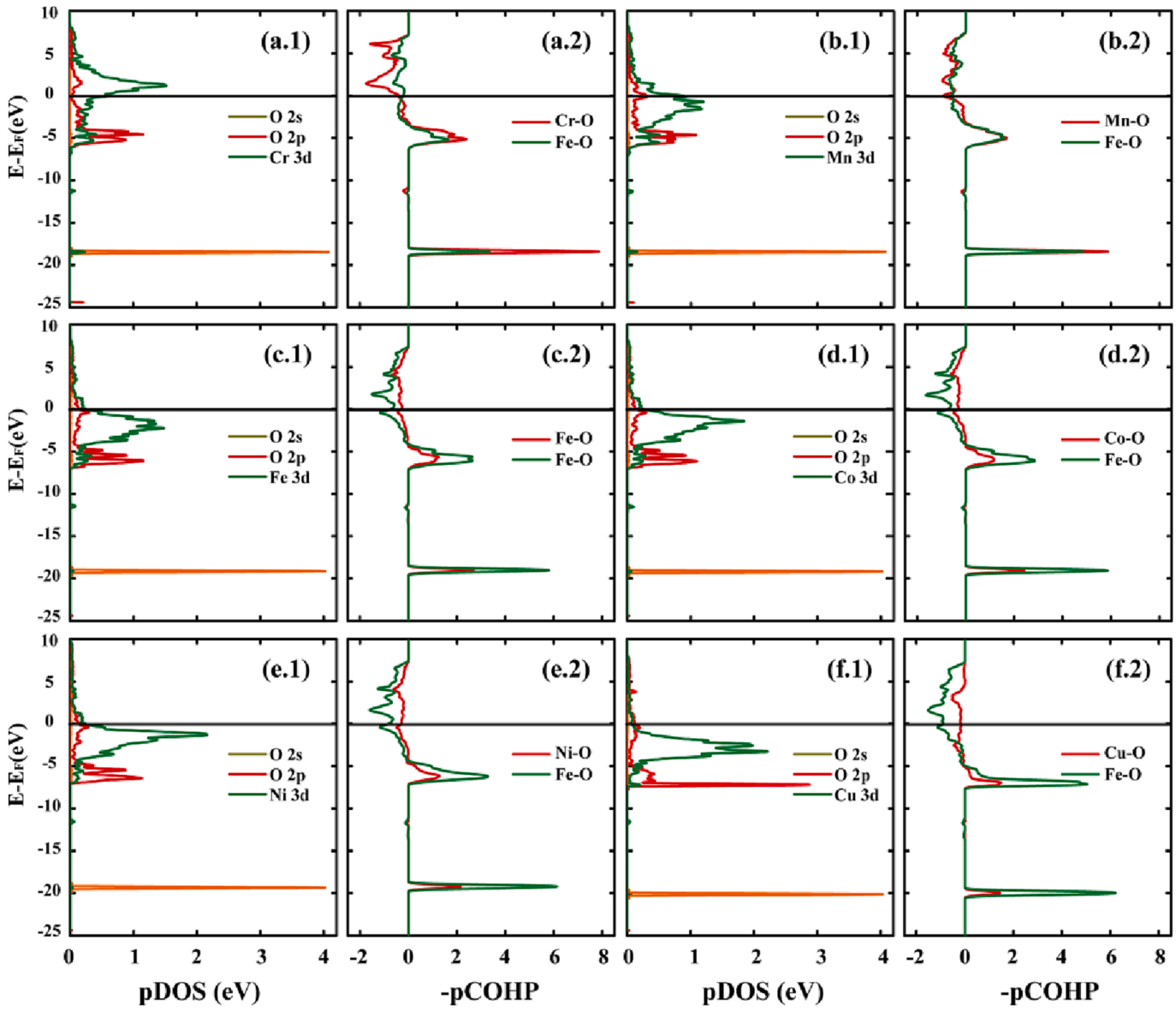

Fig. 11. pDOS and pCOHP curves for adsorbed O on the pure and M modified Fe_5C_2(100) surfaces. The pDOS and pCOHP curves for the Cr/Mn/Fe/Co/Ni/Cu substituted surfaces are shown in (a.1/a.2), (b.1/b.2), (c.1/c.2), (d.1/d.2), (e.1/e.2), and (f.1/f.2), respectively.

efficiency.

CRediT authorship contribution statement

Huiyong Gong: Data curation, Visualization, Formal analysis, Writing – original draft. **Xiaoze Yuan:** Formal analysis, Writing – review & editing. **Ming Qing:** Formal analysis, Writing – review & editing. **Jinjia Liu:** . **Xiao Han:** Writing – review & editing. **Hong Wang:** Funding acquisition, Project administration. **Xiao-Dong Wen:** Conceptualization, Resources, Supervision. **Yong Yang:** Conceptualization, Resources, Supervision, Funding acquisition. **Yongwang Li:** Project administration, Supervision.

Declaration of Competing Interest

The authors declare that they have no known competing financial interests or personal relationships that could have appeared to influence the work reported in this paper.

Data availability

No data was used for the research described in the article.

Acknowledgments

The authors are grateful for the financial support from National Key R&D Program of China (2022YFB4101202), National Science Fund for Distinguished Young Scholars (22025804, 22225206) and National Natural Science Foundation of China (22202224). We also acknowledge the State Key Laboratory of Coal Conversion, Institute of Coal Chemistry, University of Chinese Academy of Sciences and Synfuels China, Co. Ltd. for financial support.

Appendix A. Supplementary material

Supplementary data to this article can be found online at https://doi.org/10.1016/j.apsusc.2023.158088.

References

[1] F. Fischer, H. Tropsch, Über die herstellung synthetischer olgemische (synthol) durch aufbau aus kohlenoxid und wasserstoff, Brennst. Chem. 4 (1923) 276–285, https://doi.org/10.1002/cber.19230561119.

[2] F. Fischer, H. Tropsch, Die erdölsynthese bei gewöhnlichem druck aus den vergasungsprodukten der kohlen, Brennst. Chem. 7 (1926) 97–116, https://doi.org/10.1002/cber.19260590442.

[3] G.W. Huber, S. Iborra, A. Corma, Synthesis of transportation fuels from biomass chemistry, catalysts, and engineering, Chem. Rev. 106 (2006) 4044–4098, https://doi.org/10.1021/cr068360d.

[4] C. Yang, B. Zhao, D. Ma, Construction of synergistic Fe_5C_2/Co heterostructured nanoparticles as an enhanced low temperature Fischer–Tropsch synthesis catalyst, ACS Catal. 7 (2017) 5661–5667, https://doi.org/10.1021/acscatal.7b01142.

[5] Y. Yang, H.W. Xiang, Y.Y. Xu, L. Bai, Y.W. Li, Effect of potassium promoter on precipitated iron-manganese catalyst for Fischer-Tropsch synthesis, Appl. Catal. A 266 (2004) 181–194, https://doi.org/10.1016/j.apcata.2004.02.018.

[6] E. de Smit, B.M. Weckhuysen, The renaissance of iron-based Fischer-Tropsch synthesis: on the multifaceted catalyst deactivation behaviour, Chem. Soc. Rev. 37 (2008) 2758–2781, https://doi.org/10.1039/b805427d.

[7] Q. Chang, C.H. Zhang, C.W. Liu, Y.X. Wei, A.V. Cheruvathur, A.L. Dugulan, J. W. Niemantsverdriet, X.W. Liu, Y.R. He, M. Qing, L.R. Zheng, Y.F. Yun, Y. Yang, Y. W. Li, Relationship between iron carbide phases (ε-Fe_2C, Fe_7C_3, and χ-Fe_5C_2) and catalytic performances of Fe/SiO_2 Fischer-Tropsch catalysts, ACS Catal. 8 (2018) 3304–3316, https://doi.org/10.1021/acscatal.7b04085.

[8] T.A. Wezendonk, X.h. Sun, A.I. Dugulan, A.J.F. van Hoof, E.J.M. Hensen, F. Kapteijn, J. Gascon, Controlled formation of iron carbides and their performance in Fischer-Tropsch synthesis, J. Catal. 362 (2018) 106–117, https://doi.org/10.1016/j.jcat.2018.03.034.

[9] C. Yang, H. Zhao, Y. Hou, D. Ma, Fe_5C_2 nanoparticles: a facile bromide-induced synthesis and as an active phase for Fischer-Tropsch synthesis, J. Am. Chem. Soc. 134 (2012) 15814–15821, https://doi.org/10.1021/ja305048p.

[10] H. Zhao, J.X. Liu, C. Yang, S. Yao, H.Y. Su, Z. Gao, M. Dong, J. Wang, Y. Hou, W. X. Li, D. Ma, Synthesis of iron-carbide nanoparticles: identification of the active phase and mechanism of Fe-based Fischer-Tropsch synthesis, CCS Chem. 3 (2020) 2712–2724, https://doi.org/10.31635/ccschem.020.202000555.

[11] X. Liu, C. Zhang, Y. Li, J.W. Niemantsverdriet, J.B. Wagner, T.W. Hansen, Environmental transmission electron microscopy (ETEM) studies of single iron nanoparticle carburization in synthesis gas, ACS Catal. 7 (2017) 4867–4875, https://doi.org/10.1021/acscatal.7b00946.

[12] Y. Yang, H.W. Xiang, R.L. Zhang, B. Zhong, Y.W. Li, A highly active and stable Fe-Mn catalyst for slurry Fischer-Tropsch synthesis, Catal. Today 106 (2005) 170–175, https://doi.org/10.1016/j.cattod.2005.07.127.

[13] Y. Yang, H.W. Xiang, L. Tian, H. Wang, C.H. Zhang, Z.C. Tao, Y.Y. Xu, B. Zhong, Y. W. Li, Structure and Fischer-Tropsch performance of iron-manganese catalyst incorporated with SiO_2, Appl. Catal. A 284 (2005) 105–122, https://doi.org/10.1016/j.apcata.2005.01.025.

[14] D.B. Bukur, L. Nowicki, R.K. Manne, X.S. Lang, Activation studies with a precipitated iron catalyst for Fischer-Tropsch synthesis: II. Reaction studies, J. Catal. 155 (1995) 366–375, https://doi.org/10.1006/jcat.1995.1218.

[15] D.J. Duvenhage, N.J. Coville, Deactivation of a precipitated iron Fischer-Tropsch catalyst-a pilot plant study, Appl. Catal. A 298 (2006) 211–216, https://doi.org/10.1016/j.apcata.2005.10.009.

[16] L.D. Mansker, Y. Jin, D.B. Bukur, A.K. Datye, Characterization of slurry phase iron catalysts for Fischer-Tropsch synthesis, Appl. Catal. A 186 (1999) 277–296, https://doi.org/10.1016/S0926-860X(99)00149-0.

[17] D.B. Bukur, L. Nowicki, R.K. Manne, X.S. Lang, Activation studies with a precipitated iron catalyst for Fischer-Tropsch synthesis, J. Catal. 155 (1995) 366–375, https://doi.org/10.1006/jcat.1995.1218.

[18] G.B. Raupp, W.N. Delgass, Mössbauer investigation of supported Fe and FeNi catalysts: II. Carbides formed Fischer-Tropsch synthesis, J. Catal. 58 (1979) 348–360, https://doi.org/10.1016/0021-9517(79)90274-4.

[19] H. Hayakawa, H. Tanaka, K. Fujimoto, Studies on precipitated iron catalysts for Fischer-Tropsch synthesis, Appl. Catal. A 310 (2006) 24–30, https://doi.org/10.1016/j.apcata.2006.04.045.

[20] D. Mahajan, P. Gütlich, J. Ensling, K. Pandya, U. Stumm, P. Vijayaraghavan, Evaluation of nanosized iron in slurry-phase Fischer-Tropsch synthesis, Energy Fuel 17 (2003) 1210–1221, https://doi.org/10.1021/ef0300343.

[21] W. Ning, N. Koizumi, C. Hai, T. Mochizuki, T. Itoh, M. Yamada, Phase transformation of unpromoted and promoted Fe catalysts and the formation of carbonaceous compounds during Fischer-Tropsch synthesis reaction, Appl. Catal. A 312 (2006) 35–44, https://doi.org/10.1016/j.apcata.2006.06.025.

[22] P. Thüne, P. Moodley, F. Scheijen, H. Fredriksson, R. Lancee, J. Kropf, J. Miller, J. W. Niemantsverdriet, The effect of water on the stability of iron oxide and iron carbide nanoparticles in hydrogen and syngas followed by in situ X-ray absorption spectroscopy, J. Phys. Chem. C 116 (2012) 7367–7373, https://doi.org/10.1021/jp210754k.

[23] S.Z. Li, R.J. O'Brien, G.D. Meitzner, H. Hamdeh, B.H. Davis, E. Iglesia, Structural analysis of unpromoted Fe-based Fischer-Tropsch catalysts using X-ray absorption spectroscopy, Appl. Catal. A 219 (2001) 215–222, https://doi.org/10.1016/S0926-860X(01)00694-9.

[24] R. Gao, D.B. Cao, Y. Yang, Y.W. Li, J.G. Wang, H.J. Jiao, Adsorption and energetics of H_2O molecules and O atoms on the χ-Fe_5C_2(111), (−411) and (001) surfaces from DFT, Appl. Catal. A 475 (2014) 186–194, https://doi.org/10.1016/j.apcata.2014.01.032.

[25] W.S. Ning, N. Koizumi, H. Chang, T. Mochizuki, T. Itoh, M. Yamada, Phase transformation of unpromoted and promoted Fe catalysts and the formation of carbonaceous compounds during Fischer-Tropsch synthesis reaction, Appl. Catal. A 312 (2006) 35–44, https://doi.org/10.1016/j.apcata.2006.06.025.

[26] D. Li, C. Zhou, X. Shi, Q. Zhang, Q. Song, Y. Zhou, D. Jiang, PtAg alloys as an efficient co-catalyst for CO_2 deep photoreduction with H_2O: synergistic effects of Pt and Ag, Appl. Surf. Sci. 598 (2022), https://doi.org/10.1016/j.apsusc.2022.153843.

[27] Y. Yu, J. Lu, W. Zhang, K. Yang, M. Zhang, Theoretical insight into the mechanism of CO_2 and H_2O formation from CO and OH over stepped Ni and Fe/Ni bimetallic surfaces, Appl. Surf. Sci. 615 (2023), https://doi.org/10.1016/j.apsusc.2022.156320.

[28] H. Li, J. Jelic, F. Studt, The barrier free splitting of O-H bond in H_2O and CH_3OH due to the synergetic effects of single atom (Cu1/Fe1) coordination change and ZnO(110) surface oxygen activation, Appl. Surf. Sci. 576 (2022), https://doi.org/10.1016/j.apsusc.2021.151750.

[29] M. Zhang, S. Chi, H. Huang, Y. Yu, Mechanism insight into MnO for CO activation and O removal processes on Co(0001) surface: a DFT and KMC study, Appl. Surf. Sci. 567 (2021), https://doi.org/10.1016/j.apsusc.2021.150854.

[30] W. Ma, E.L. Kugler, D.B. Dadyburjor, Promotional effect of copper on activity and selectivity to hydrocarbons and oxygenates for Fischer-Tropsch synthesis over potassium-promoted iron catalysts supported on activated carbon, Energy Fuel 25 (2011) 1931–1938, https://doi.org/10.1021/ef101720c.

[31] E. De Smit, F.M. De Groot, R. Blume, M. Havecker, A. Knop-Gericke, B. M. Weckhuysen, The role of Cu on the reduction behavior and surface properties of Fe-based Fischer-Tropsch catalysts, PCCP 12 (2010) 667–680, https://doi.org/10.1039/b920256k.

[32] A. Loaiza-Gila, B. Fontalb, F. Ruedac, J. Mendialduac, R. Casanovac, On carbonaceous deposit formation in carbon monoxide hydrogenation on a natural iron catalyst, Appl. Catal. A 177 (1999) 193–203, https://doi.org/10.1016/S0926-860X(98)00260-9.

[33] D. Peña, L. Jensen, A. Cognigni, R. Myrstad, T. Neumayer, W. van Beek, M. Rønning, The effect of copper loading on iron carbide formation and surface species in iron-based Fischer-Tropsch synthesis catalysts, ChemCatChem 10 (2018) 1300–1312, https://doi.org/10.1002/cctc.201701673.

[34] S.D. Qin, C.H. Zhang, J. Xu, B.S. Wu, H.W. Xiang, Y.W. Li, Mo and Cu modified FeK/SiO_2 catalysts for Fischer-Tropsch synthesis, Chin. J. Catal. 31 (2010) 1132–1138, https://doi.org/10.3724/SP.J.1088.2010.00142.

[35] S.l. Liu, Y.W. Li, J.G. Wang, H.J. Jiao, Mechanisms of H_2O and CO_2 formation from surface oxygen reduction on Co(0001), J. Phys. Chem. C 120 (2016) 19265–19270, https://doi.org/10.1021/acs.jpcc.6b06649.

[36] H. Xiong, L.L. Jewell, N.E.J. Coville, Shaped carbons as supports for the catalytic conversion of syngas to clean fuels, ACS Catal. 5 (2015) 2640–2658, https://doi.org/10.1021/acscatal.5b00090.

[37] H. Gong, Y. He, J. Yin, S. Liu, M. Qing, Q. Peng, C.-F. Huo, H. Wang, Y. Yang, X. D. Wen, Electronic effects of transition metal dopants on Fe(100) and Fe_5C_2(100) surfaces for CO activation, Catal, Sci. Technol. 10 (2020) 2047–2056, https://doi.org/10.1039/c9cy02428j.

[38] G. Kresse, J. Furthmüller, Efficiency of ab-initio total energy calculations for metals and semiconductors using a plane-wave basis set, Comp. Mater. Sci. 6 (1996) 15–50, https://doi.org/10.1016/0927-0256(96)00008-0.

[39] G. Kresse, J. Furthmüller, Efficient iterative schemes for ab initio total-energy calculations using a plane-wave basis set, Phys. Rev. B: Condens. Matter and Mater. Phys. 54 (1996) 11169–11186, https://doi.org/10.1016/0927-0256(96)00008-0.

[40] P.E. Blochl, Projected augmented-wave method, Phys. Rev. B: Condens. Matter Mater. Phys. 50 (1994) 17953–17979, https://doi.org/10.1103/PhysRevB.50.17953.

[41] J.P. Perdew, K. Burke, M. Ernzerhof, Generalized gradient approximation made simple, Phys. Rev. Lett. 77 (1996) 3865–3868, https://doi.org/10.1103/PhysRevLett.77.3865.

[42] J.P. Perdew, Y. Wang, Accurate and simple analytic representation of the electron-gas correlation energy, Phys. Rev. B 45 (1992) 13244–13249, https://doi.org/10.1103/PhysRevB.98.079904.

[43] G. Henkelman, H. Jónsson, Improved tangent estimate in the nudged elastic band method for finding minimum energy paths and saddle points, J. Phys. Chem. 113 (2000) 9978–9985, https://doi.org/10.1063/1.1323224.

[44] G. Henkelman, B.P. Uberuaga, H. Jónsson, A climbing image nudged elastic band method for finding saddle points and minimum energy paths, J. Phys. Chem. 113 (2000) 9901–9904, https://doi.org/10.1063/1.1329672.

[45] S. Zhao, X.W. Liu, C.F. Huo, Y.W. Li, J.G. Wang, H.J. Jiao, Surface morphology of Hägg iron carbide (χ-Fe_5C_2) from ab initio atomistic thermodynamics, J. Catal. 294 (2012) 47–53, https://doi.org/10.1016/j.jcat.2012.07.003.

[46] R. Dronskowski, P.E. Bloechl, Crystal orbital Hamilton populations (COHP): energy-resolved visualization of chemical bonding in solids based on density-functional calculations, J. Phys. Chem. 97 (1993) 8617–8624, https://doi.org/10.1021/j100135a014.

[47] V.L. Deringer, A.L. Tchougréeff, R. Dronskowski, Crystal orbital hamilton population (COHP) analysis as projected from plane-wave basis sets, Chem. A Eur. J. 115 (2011) 5461–5466, https://doi.org/10.1021/jp202489s.

[48] S. Maintz, V.L. Deringer, A.L. Tchougreeff, R. Dronskowski, Analytic projection from plane-wave and PAW wavefunctions and application to chemical-bonding analysis in solids, J. Comp. Chem. 34 (2013) 2557–2567, https://doi.org/10.1002/jcc.23424.

[49] K. Reuter, M. Scheffler, Composition and structure of the RuO_2(110) surface in an O_2 and CO environment: implications for the catalytic formation of CO_2, Phys. Rev.

B: Condens. Matter Mater. Phys. 68 (2003), https://doi.org/10.1103/PhysRevB.68.045407.
[50] F. Zasada, W. Piskorz, S. Cristol, J.F. Paul, A. Kotarba, Z. Sojka, Periodic density functional theory and atomistic thermodynamic studies of cobalt spinel nanocrystals in wet environment: molecular interpretation of water adsorption equilibria, J. Phys. Chem. C 114 (2010) 22245–22253, https://doi.org/10.1021/jp109264b.
[51] W. Piskorz, J. Grybos, F. Zasada, P. Zapała, S. Cristol, J.F. Paul, Z. Sojka, Periodic DFT study of the tetragonal ZrO_2 nanocrystals: equilibrium morphology modeling and atomistic surface hydration thermodynamics, J. Phys. Chem. C 116 (2012) 19307–19320, https://doi.org/10.1021/jp3050059.
[52] T. Zeng, X.D. Wen, Y.W. Li, H. Jiao, Density functional theory of triangular molybdenum sulfide nanocluster and CO adsorption on it, J. Phys. Chem. B 109 (2005) 13704–13710, https://doi.org/10.1021/jp0518153.
[53] Y. Meng, X.Y. Liu, Y.J. Ma, X.H. Gao, X.D. Wen, Investigation of water gas shift reactivity on Fe_5C_2 (111): a DFT study, Mol. Catal. 529 (2022), https://doi.org/10.1016/j.mcat.2022.112538.
[54] C.H. Zhang, Y. Yang, B.T. Teng, T.Z. Li, Z.H. Yan, H.W. Xiang, Y.W. Li, Study of an iron-manganese Fischer-Tropsch synthesis catalyst promoted with copper, J. Catal. 237 (2006) 405–415, https://doi.org/10.1016/j.jcat.2005.11.004.
[55] D.B. Cao, F.Q. Zhang, Y.W. Li, J.G. Wang, H.J. Jiao, Density functional theory study of hydrogen adsorption on Fe_5C_2(001), Fe_5C_2(110), and Fe_5C_2(100), J. Phys. Chem. B 109 (2005) 833–844, https://doi.org/10.1021/jp046239+.
[56] J. Yang, Y.C. Sun, Y. Tang, Y. Liu, H.L. Wang, L. Tian, H. Wang, Z.X. Zhang, H. W. Xiang, Y.W. Li, Effect of magnesium promoter on iron-based catalyst for Fischer-Tropsch synthesis, J. Mol. Catal. A Chem. 245 (2006) 26–36, https://doi.org/10.1016/j.molcata.2005.08.051.
[57] H. Gong, M. Qing, H. Wan, X. Yuan, P. Qiao, X. Liu, X. Song, B. Wu, H. Wang, X.-D. Wen, Y. Yang, Y.-W. Li, Fe-Sn bimetallic catalysts for an enhanced Fischer-Tropsch synthesis stability via oxygen removal and coking resistance, Fuel 311 (2022), https://doi.org/10.1016/j.fuel.2021.122115.